Quasiparticle diffusion and the energy resolution of superconducting tunneling junctions as photon detectors. II. Experiment

Roland den Hartog
Astrophysics Division, European Space Agency–ESTEC, Noordwijk, Netherlands

A. G. Kozorezov and J. K. Wigmore
School of Physics and Chemistry, Lancaster University, Lancaster, United Kingdom

D. Martin, P. Verhoeve, A. Peacock, A. Poelaert, and G. Brammertz
Astrophysics Division, European Space Agency–ESTEC, Noordwijk, Netherlands

(Received 20 July 2001; revised manuscript received 4 April 2002; published 13 September 2002)

In a previous paper we presented an analytical iterative model to describe the spectral characteristics of a superconducting tunnel junction (STJ) used as a photon detector, in terms of the spatial and temporal evolution of the quasiparticle population in both electrodes. This model includes effects from quasiparticle recombination, multiple quasiparticle tunneling, phonon coupling between the electrodes, asymmetry between base and counter electrode, losses at nonideal edges and diffusive losses into electrical connections, bridges, or localized traps. Here we discuss two examples in which this model is applied to comprehensive experimental datasets obtained with multiple STJ's, and demonstrate how this model can be used to obtain a better understanding of the factors that limit the energy resolution in STJ's as photon detectors.

DOI: 10.1103/PhysRevB.66.094511 PACS number(s): 74.25.Fy, 85.25.Oj, 73.50.Gr, 85.25.Am

I. INTRODUCTION

Although the measured energy resolution of superconducting tunnel junctions (STJ's) used as photon detectors approaches the theoretical limit at optical and UV energies, in the x-ray regime there remains a significant discrepancy, the origin of which is not well understood. The best results are an intrinsic energy resolution for 6 keV photons of 29 eV for Nb/Al STJ's,[1] 16 eV for Ta both in a single STJ with collimated illumination,[2] and a strip absorber,[3] and 10 eV for Al.[4] However, these results are still at least a factor 2 above the resolution arising from statistical fluctuations in the creation[5] and tunneling of the quasiparticles,[6,7] respectively, 10, 7, and 4 eV for the above materials.

In the previous paper[8]—hereafter paper I—we discussed the possibility that a significant, additional contribution to x-ray linewidth may be due to inhomogeneous broadening, that is, to a dependence of the responsivity of an STJ on the position of the photoabsorption event. We presented an analytical, iterative model of the response surface for an STJ in terms of the spatial and temporal evolution of the quasiparticle population in the two (nonidentical) electrodes. The effects of all significant mechanisms for quasiparticle interaction and loss were included, notably, multiple tunneling, recombination, phonon coupling, diffusive transport into leads and bridges, and trapping at nonideal edges and localized traps.

In the present paper we make a detailed, quantitative comparison of the model with experimental results obtained from two different sets of STJ's; the first a sequence of single STJ's differing only in size, and the second a 3×3 array of devices connected by bridges. Earlier indications that spatial inhomogeneity may influence STJ resolution have been obtained in a number of previous investigations, both theoretically[9–13] and experimentally. In experiments using low-temperature scanning electron microscopy (LTSEM),[14–16] and the recently developed low-temperature scanning synchrotron microscopy (LTSSM),[17] it was possible to observe directly the spatial variation of responsivity. From analysis of the responsivity of STJ arrays there exists also experimental evidence that the actual loss sites which dominate the spatial response of STJ's are localized.[3,16] In particular, the positioning of lead connections have a major impact on the inhomogeneity of the response.

Because the model involves a considerable number of input parameters, it is important to use datasets that are sufficiently comprehensive to provide useful restrictions on all input parameters. In this paper we discuss two such datasets. One was obtained for a set of five single STJ's of different sizes (sample 1), for which LTSEM data and spectral data, obtained by illumination with an Fe^{55} source, are available. The second set of data was obtained with an array of 3×3 STJ's (sample 2), of which the base electrodes are connected via small bridges. Spectral data was obtained at several energies, including the *L* and *K* lines of Cu and Fe targets. Simultaneous read outs of one STJ and its two neighbors allowed us to obtain detailed knowledge of the charge losses across the bridges (cross talk). We demonstrate that both cases satisfy the requirements of the model for the linear superposition of perturbations, and that almost all features of these complicated datasets are accurately reproduced.

II. EXPERIMENT

A. Fabrication

The STJ's used in our experiments were fabricated by Oxford Instruments, UK, and VTT Electronics, Finland, as part of an ongoing effort by ESA to develop imaging spectroscopic detectors for astronomical purposes.[18] The sand-

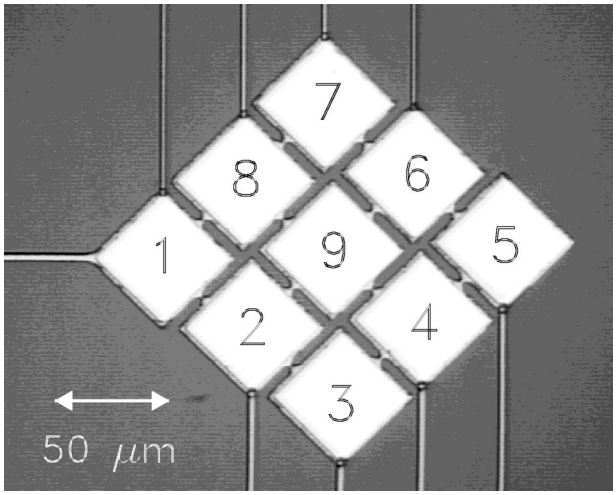

FIG. 1. Top view Nomarski microscope image of the 3×3 array of Nb-based STJ's (sample 2), with a definition of the numbering. Note that the top electrode of the central pixel (No. 9) of the Nb array is not connected. All other connections are intact.

wiches of Nb/Al/AlO_x/Al/Nb were magnetron sputtered on a superpolished sapphire substrate in one run without breaking the vacuum in the deposition chamber. Deposition conditions were selected such that the first Nb overlayer is epitaxial with the sapphire, and the first Al layer epitaxial with the Nb. Exposure of the first Al layer to a controlled amount of oxygen creates the AlO_x barrier, with a typical resistivity of $2.5\pm0.5\ \mu\Omega\ \mathrm{cm}^2$. The layers that are deposited on top of the barrier are polycrystalline. The manufacturing processes of the STJ's are modified versions of the SNEP technique.[19,20] The main difference between the fabrication processes of sample 1 (Oxford Instruments) and sample 2 (VTT) lies in the etching of the trilayer; where Oxford Instruments applies a wet etch technique, VTT uses a reactive ion etching technique.

The single STJ's of sample 1 are part of a series of 8 devices with different sizes (10, 20, 50, and 100 μm) and different lead widths (1 and 3 μm), all deposited on the same sapphire substrate. The Nb base electrode is 110 nm thick, monocrystalline epitaxial with the substrate, and has a residual resistance ratio $(\mathrm{RRR})=\rho_{293\ \mathrm{K}}/\rho_{10\ \mathrm{K}}=109$. As the diffusion constant scales proportional with the RRR, this value suggests fast quasiparticle diffusion in the base film. The first Al layer is 5-nm thick, and epitaxial with the Nb base film. On top of the barrier is another 5-nm-thick layer of Al, polycrystalline, with an average grain diameter of 40 nm (estimated from TEM cross-sectional images). The top Nb electrode is 180 nm thick and polycrystalline. The top electrode has an (estimated) RRR value of 4. Clearly, the diffusion of quasiparticles in the top electrode will be considerably slower than in the base electrode. The average energy gap of the combined electrodes is 1.37 meV, which is 12% lower than the bulk Nb value due to the proximity effect of the Al layer.

Figure 1 shows a picture of the 3×3 array of STJ's in sample 2, including the numbering convention. As this array was mainly intended as a technology demonstrator, the top electrode of the central STJ (No. 9) was not connected and the width of the remaining top lead connections and the number of bridges varies among the STJ's. The top-film lead connections are 2 μm wide for STJ's 2, 3, 4, 5, and 1 μm wide for STJ's 1, 6, 7, 8. The width of the base lead to STJ 1 is 2 μm, as is the nominal length and width of the bridge connections between adjacent STJ's. The odd numbered STJ's have 2 bridge connections to their neighbors and the even numbered STJ's have three bridge connections. The base electrode of the STJ's in the array consists again of monocrystalline Nb, epitaxial with the sapphire substrate, and has dimensions $44\times44\times0.10\ \mu\mathrm{m}^3$. On top of the base electrode lies a sandwich consisting of 10 nm Al, epitaxial with the Nb, a barrier of ~1.9 nm AlO_x and another 10 nm Al, which together with a Nb layer forms the polycrystalline top electrode. The dimensions of the top electrode are $40\times40\times0.25\ \mu\mathrm{m}^3$. As a consequence, the STJ has a ''mesa'' structure, with the base electrode being slightly larger than the top electrode. Hence there is a 2 μm wide rim around the base electrode from which quasiparticles cannot directly tunnel into the top electrode (see also Fig. 1 in paper I). Due to the thicker Al layers, the energy gap Δ is lower than in the previous case, 1.15–1.19 meV. Several RRR measurements were performed to assess the quality of the films in the stack in detail. The full stack of layers had an RRR value of 25. Two separate depositions of single Nb layers have been made under conditions and with thickness identical to those of the the base and the top Nb depositions in the stack. These layers had RRR values of 61 and 12 for base and top Nb, respectively. Assuming that the ratio of the RRR values of the Al layers in the base and top electrode is the same as for the Nb layers, and the resistances of the layers in the stack can be added as parallel resistors, we find for base and top electrode RRR values of 41 and 8, respectively.

B. Experimental conditions

All the spectral measurements are carried out in two cryostats with base temperatures of about 1.25 K. A magnetic field of typically 100 G, parallel with the barrier and at 45° with the sides of the electrode, is applied to suppress the dc (and, as much as possible, the ac) Josephson current. A voltage bias of typically 0.5 mV is applied to keep the STJ's at the point where the S/N ratio is maximum. This point corresponds roughly to the maximum in the tunnel current, as the electronic noise is the dominating noise source here, but usually an offset is applied to stay clear from Fiske steps (see Fig. 2). The current pulses from the detectors are processed on-line through a charge-sensitive preamplifier with low-noise JFET input stages, followed by electronic shaping with two bipolar semi-Gaussian filters into a fast (triggering) channel and a slow channel that corresponds to the integrated charge. The information in the fast and slow channels encodes also the pulse duration. Pulses can be collected in coincidence for up to four channels. An electronic pulser is coupled in during the measurements to assess the noise from the detector environment (pick-up on cables, amplifier noise, IR background).

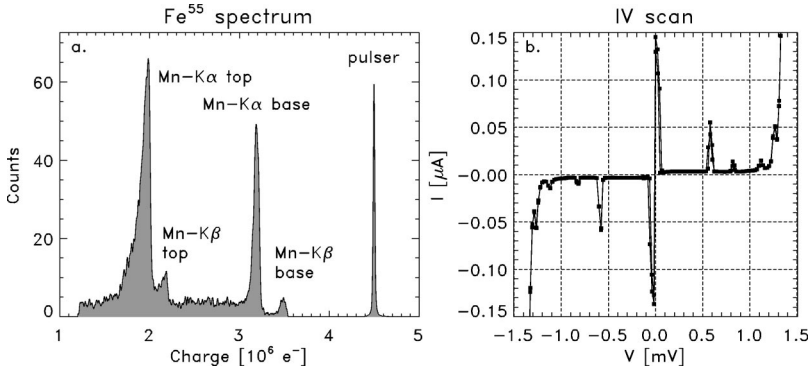

FIG. 2. (a) Fe^{55} spectrum, including pulser, obtained with the 50 μm single STJ (sample 1) with 1 μm wide leads. The main spectral features are identified. Top and base film FWHM energy resolutions are 353 and 127 eV, respectively. (b) Current-voltage characteristic taken under the same circumstances, showing the subgap current at a level of 5 nA, and the residual ac and dc Josephson currents.

C. Data

Our datasets generally consist of two parts. One part corresponds to some representation of the response surface (charge output as a function of photon absorption position), either in the form of a LTSEM scan, or in the form of spectral line profiles (or both), while the other part consists of measurements of the duration time of the charge pulse from the STJ. Both parts are reproduced by the theory described in paper I.

1. A series of single STJ's

Fe^{55} spectra were obtained for four STJ's in sample 1, with sizes of 10, 20, 50, and 100 μm respectively, and 1 μm wide leads. Figure 2(a) shows an example of such a spectrum, including the pulser signal, which monitors the electronic noise. Additional LTSEM scans on the two 50 μm STJ's of sample 1 (respectively, with 1- and 3-μm-wide leads) were carried out at the University of Tübingen. An overview of STJ properties and corresponding data used in this paper is given in Table I.

Figure 2 provides examples of a typical Fe^{55} spectra, and a corresponding current-voltage characteristic. An example of a LTSEM scan is shown in Fig. 3. It provides an accurate impression of the response surface for electrons absorbed in the top film. In particular the impact of the lead is clearly demonstrated. The image resolution is limited to 100 nm due to the necessity to apply a magnetic field for suppression of the Josephson current. STJ response signal inhomogeneities larger than 3% can be detected. The base temperature of the integrated cryostat was 1.6 K, which is still an acceptable temperature for Nb STJ's with thin Al layers. The scans were made with a beam energy of 5 keV to ensure only stimulation of the top film. A disadvantage of this technique is the inability to stimulate the base film without evoking a response from the top film as well, which limits this technique to analysis of the top electrode. Although the processes of photon and electron absorption are physically different, the timescale on which the quasiparticle cloud is generated is so short compared to other characteristic timescales (tunnel time, diffusive crossing time),[21] that no detectable differences are to be expected. In LTSEM the electron beam is normal to the electrode, while after irradiation with x rays of comparable energy (LTSSM), the photoelectrons initially move parallel to the film. However, we do not expect significant differences in the production of nonequilibrium quasiparticles in LTSEM and LTSSM because at 5 keV the photoelectron range in Nb is 120 nm, smaller than the thickness of the top Nb film.

2. An array of coupled STJ's

Sample 2 was characterized inside a portable cryostat on our soft x-ray beamline. X rays were generated with a Manson 5 source on a Cu target (Cu-*L* line, 930 eV), and Trufocus source tubes with Fe and Cu targets (Fe-*K* and Cu-*K*, 6395 and 8037 eV, respectively). The dataset is summarized in Table I.

In Fig. 4 a comparison is made between the spectral features for the 8 STJ's that are connected. Figures 4(a) and 4(d) imply that the charge output of both the base and top electrodes depends strongly on the number of bridges connected to the base films. Figure 4(c) indicates that per bridge slightly less than 6% of the total number of quasiparticles

TABLE I. Summary of properties and available datasets for STJ's in both samples. An asterisk indicates LTSEM scans.

	Sample 1					Sample 2							
STJ	1	2	3a	3b	4	1	2	3	4	5	6	7	8
top film size (μm)	10	20	50	50	100	40	40	40	40	40	40	40	40
base film size (μm)	10	20	50	50	100	44	44	44	44	44	44	44	44
lead width (μm)	1	1	1	3	1	1	2	2	2	2	1	1	1
number of bridges						2	3	2	3	2	3	2	3
energy (keV)	5.9	5.9	5.9		5.9	6.5	6.5	6.5	6.5	6.5	6.5	6.5	6.5
add. energy (keV)			5.0*	5.0*						0.93	0.93	0.93	
add. energy (keV)										8.0	8.0	8.0	

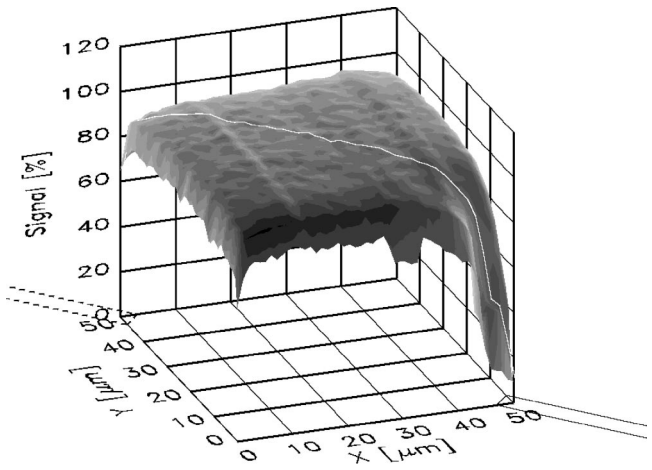

FIG. 3. LTSEM scan with 5 keV electrons of the response surface of the top electrode of a 50 μm STJ (sample 1) with a 3 mm wide lead. The impact of the top lead on the shape of the response surface is clearly demonstrated. The stripes in the *y* direction (scanning direction) across the surface are instrumental artifacts. On the base surface the lead connections to the top electrode (solid lines) and base electrode (dashed lines) are indicated. The signal is normalized to the center of the electrode. The white line across the surface indicates the one-dimensional cross section of the scan to which the model is fitted.

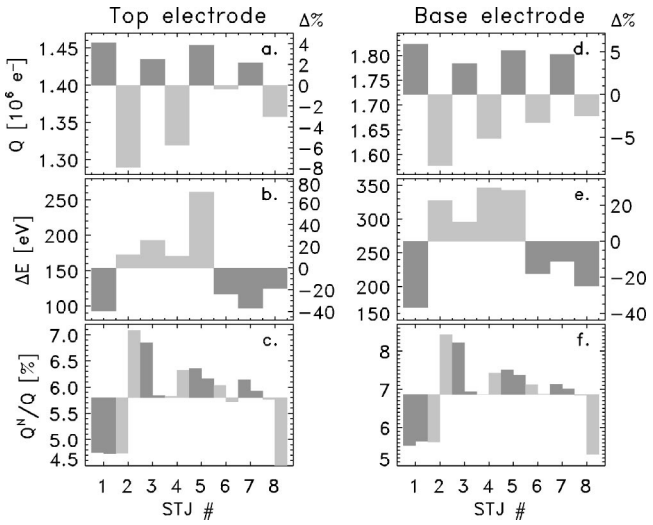

FIG. 4. Side-by-side comparison of the properties of the eight connected STJ's in sample 2. All values were obtained for 6490 eV x rays from a Fe target. (a) Charge-output signal detected in the top electrodes where the photons are absorbed. Gray scale coding indicates number of bridges connected to the base electrode: dark shading indicates two bridge connections, light shading, three. (b) Energy resolution, gray scale coded for the width of the top lead connection: dark shading indicates 1 μm width, light shading 2 μm. (c) Cross-talk signals detected by the two neighbor STJ's, Q^N, as a percentage of the total charge signal Q (corrected for losses across the bridges). Gray scale coding same as under (a). (d)–(f) *Idem*, for photons absorbed in the base electrodes.

that are detected through tunneling escape. For quasiparticles created in the base film this fraction appears larger, almost 7% according to Fig. 4(f), because here quasiparticles can escape across the bridges before having tunneled. These quasiparticles do not contribute to the measured charge output of the electrode, but do show up in the cross-talk signal. The energy resolution, on the other hand, does not seem to depend so much on the number of bridges as on the width of the top lead connection, as is apparent from Figs. 4(b) and 4(e). On the other hand, the effect of lead width on the charge output is less pronounced. Comparison of the charge outputs of top electrodes with 1- and 2-μm-wide leads suggests a 2% effect on the total charge output. So the key question arises why the bridges, which have a substantial influence on the charge output, have hardly an impact on the energy resolution, while the top leads, which hardly affect the charge output, have such a dramatic effect on the energy resolution.

Finally, the additional 2-μm-wide ground lead connected to the base film does not seem to have a negative influence on the charge output at all. On the contrary, the charge output of STJ 1 is the highest among the STJ's. Figures 4(c) and 4(f) demonstrate clearly that the bridges between STJ 1 and its neighbors, STJ's 2 and 8, are the most inefficient conductors of the array. Still, the reduced transparency of the bridges explains only 2% of the 6% difference in charge output between STJ 1 and the average and cannot fully compensate the presence of the base lead. Apparently, hardly any quasiparticles are lost via the base lead. This is confirmed by a comparison with a reference array (not shown here). The reason is probably that the Nb in the base lead is not in contact with Al, and will therefore have a gap equal to that of bulk Nb. The proximized base electrode has a lower gap, and the quasiparticles in the electrode will be Andreev reflected by the lead (provided that they are sufficiently relaxed).

3. Pulse duration times

The current pulse $I_i(t)$ generated by the STJ as a result of a photon absorption in electrode *i* is given by Eq. (E2) in paper I. It is clear from this expression that, even when losses at the edges and through leads and traps are absent, the pulse from an STJ cannot be characterized by a single time parameter, but is dominated by two exponential decay times. Each of these decay times is a combination of four parameters, namely, the quasiparticle tunnel and loss times in the two electrodes. Usually, only one of the two dominates, so that the pulse has a quasiexponential time dependence. Even with careful sampling of the pulses by a digital oscilloscope it is difficult to separate these two exponentials. Reference 22 therefore discusses special techniques to derive the four parameters from phonon-induced pulses. The electronics used in this work, however, are geared towards a high through-put of pulses, and therefore characterize the pulses by a single duration time, that is derived from the signals in the fast and the slow channel. The ratio of the charge output in the slow channel to that in the fast contains information about the pulse duration time. This ratio is calibrated using pulser signals with well-known total charges and exact exponential decay. Although the detailed information about the double exponential form of the pulses is therefore lost, the combination of pulse duration times and charge output val-

TABLE II. Required input parameters for the components of the model. The parameters were introduced in paper I. A tick indicates that the parameter is required for the calculation of the respective contribution. Index *j*, which runs over 1 and 2, indicates that both the parameter values for base and top electrode are required.

	Fixed							Variable						
Contribution	L	d_j	N_h	r_{ini}	N_0	$\mathbf{x}_a$	$\mathbf{x}_{l,j}$	D_j	$\Gamma_{t,ij}$	$\Gamma_{l,j}$	R_j^*	R_{ij}^*	β_j	$g_{l,j}$
$S_{i,1}$	√	√	√	√	√	√		√	√	√	√	√		
$S_{i,2}$	√	√	√	√	√	√		√	√	√	√	√		
$S_{i,\text{edge}}$	√	√	√			√		√	√	√			√	
$S_{i,\text{out}}$	√	√	√			√	√	√	√	√				√
$I_i(t)$	√							√	√	√			√	√

ues for both electrodes (four values in total) provides enough information to sufficiently restrict the quasiparticle tunnel and loss times in both electrodes (four parameters).

III. MODEL

A. Description

According to the theory of paper I, the response surface is constructed from four contributions added in superposition to the flat response of an ideal detector: the first and second iteration of the nonlinear response, the contribution from quasiparticle trapping at the perimeter of the electrode, and the quasiparticle losses into leads, bridges or localized traps:

$$S_i(E,\mathbf{x}_a)=\mathbf{1}+S_{i,1}(E,\mathbf{x}_a)+S_{i,2}(E,\mathbf{x}_a)+S_{i,\text{edges}}(\mathbf{x}_a)+S_{i,\text{leads}}(\mathbf{x}_a)+S_{i,\text{bridges}}(\mathbf{x}_a), \tag{3.1}$$

where $i=1,2$ for absorption in, respectively, the top or base film. Apart from photon energy E and absorption position $\mathbf{x}_a$, each of these contributions depends on a list of input parameters, which are summarized in Table II. For the purpose of further discussion they are divided into two groups: ''fixed'' parameters, that correspond to established properties of the electrode or that determine the algorithm and ''variable'' parameters, which means that we hope to derive their values from fitting the model to data. The symbols are the same as in paper I, to which we refer for an explanation. Most parameters differ in top and base electrodes. Because both electrodes are coupled through quasiparticle tunneling and phonon transport across the barrier, both parameters are required for the computation of the respective contribution.

Starting from a response surface, the derivation of spectral lines is straightforward. The basic spectral line shape is just the histogram of the response surface. In the case of a Fe^{55} spectrum, we only consider the two main lines, Mn-K_α (5895 eV) and Mn-K_β (6490 eV). Given the energy resolutions of the detectors at hand it is not necessary to treat Mn-$K_{\alpha 1}$ and Mn-$K_{\alpha 2}$ separately; neither is the natural width of these lines of any importance.[23] For the same reason the statistical contributions from Fano and tunnel noise to the linewidth can be ignored. The STJ charge output corresponding to the Fe^{55} spectrum is then given by [see Eq. (2.14) in paper I]:

$$Q(E_{\text{Fe}^{55}})=e\{N_0(K_\alpha)[\langle n_t\rangle S_t(E_{K_\alpha})+\eta_{K_\alpha}\langle n_b\rangle S_b(E_{K_\alpha})] + 0.139N_0(K_\beta)[\langle n_t\rangle S_t(E_{K_\beta}) + \eta_{K_\beta}\langle n_b\rangle S_b(E_{K_\beta})]\}\otimes P(E). \tag{3.2}$$

Here $N_0(K_\alpha)$ and $N_0(K_\beta)$ are the initial number of quasiparticles generated upon absorption of a Mn-K_α or Mn-K_β photon; η_{K_α} and η_{K_β} are factors that correct for the photons absorbed in the top electrode, based on the mass absorption coefficients in the Henke tables.[24] The $\langle n_t\rangle$ and $\langle n_b\rangle$ are the charge multiplication factors in top and base electrode, respectively, due to multiple tunneling, and were introduced in paper I. $S_t(E)$ and $S_b(E)$ represent the spectral line shapes and are obtained by spatial integration over the (normalized) response surfaces for top and base electrode. Finally, the entire spectrum is convolved with $P(E)$, the measured pulser profile, to properly account for the electronic noise.

B. Fitting the model

1. Input parameters

The amount of freedom in the model is in reality much less than the presence of 14 free parameters in Table II suggests, since we already know the approximate values of these parameters either from first principles or from additional measurements.

The most important parameters are the diffusion constants; unfortunately these are also the least well understood. In normal-state Nb at low temperatures, they can be estimated from the RRR values of the electrodes, using the familiar Einstein relation, as $D_n=\text{RRR}/2N(0)\rho_{293}e^2 \approx 8$ RRR $\text{cm}^2\,\text{s}^{-1}$. Here $N(0)$ is the single-spin density of states in Nb, equal to 3.2×10^{22} cm^{-3} eV^{-1},[25] and ρ_{293} the room temperature resistivity of Nb (12.5 $\mu\Omega$ cm). Alternatively, the diffusion constant can be estimated by $D_n=\frac{1}{3}v_F\lambda\approx 6$ RRR $\text{cm}^2\,\text{s}^{-1}$, giving approximately the same value. Here we used the relation between normal-state resistivity and electron mean free path in Nb, $\rho_n\lambda=3.75\times10^{-6}\mu\Omega\text{cm}^2$,[26] implying $\lambda=3$ RRR nm, and a Fermi velocity of $v_F=5.7\times10^7$ cm/s.[27] Below we will use $D_n=7$ RRR cm^2s^{-1}.

Estimating the diffusion coefficient of quasiparticles in superconductors is more difficult. Quasiparticles move

with an energy dependent group velocity $v_{\mathrm{QP}}(\epsilon) = v_F\sqrt{1-(\Delta/\epsilon)^2}$, so that an average diffusion constant depends on the details of quasiparticle energy distribution. In thermal equilibrium the diffusion constant was found in Ref. 28. However, this condition does not apply to the quasiparticle populations in our detectors. A thermalized energy distribution, with quasiparticle density that still far exceeds the thermal density, requires efficient phonon exchange with the bath. At low temperatures this process is extremely slow, because the phonon population is frozen out. At temperatures as high as in our experiments (1.2 K) the characteristic single-phonon absorption time is of the order of 200–300 ns. The thermalization time is therefore of the same order of magnitude as the tunnel time. However, in each tunneling event the quasiparticle gains energy equal to eV_{bias} from the external bias source. This causes heating of the quasiparticle population and prevents the establishment of a thermalized distribution. The possibility of establishing local equilibrium within the quasiparticle system via strong scattering between quasiparticles is also excluded. The scattering time scale can be roughly estimated using the Eliasberg formula[29] $\tau_{\mathrm{QP}}^{-1} = (kT_C)^2/\hbar E_F \times n_{\mathrm{QP}}/2N(0)\Delta$. It is larger than 10 μs even for the largest density of quasiparticles in our smallest (10μ) device. Under these conditions the mean energy of the nonequilibrium quasiparticle distribution is better characterized by the so-called balance energy, defined as the quasiparticle energy at which tunnel rate is equal to the phonon emission rate.[30] Although the quasiparticle mean energy does not coincide with the balance energy and should be derived from the kinetic equation, the balance energy sets the correct time scale. This is because the quasiparticle distribution is based on a trade-off between the energy gain in tunnel processes (both for direct and back-tunneling events) and the energy loss in the inelastic scattering processes with subsequent phonon emission. For our detectors, the balance energy lies at 1.1Δ. At this energy, $\langle v_{\mathrm{QP}}\rangle \equiv 0.42\, v_F$, hence a typical estimate of the quasiparticle diffusion constant would be $D \approx 3.0$ RRR cm^2 s^{-1}. We note here that previous experimental verifications of the quasiparticle diffusion constants usually fell short of any theoretical expectation by factors ranging from 4 to 7 in Ta,[31,32] to two orders of magnitude in Nb.[33] This phenomenon has so far eluded a proper explanation, hence we take the theoretical prediction only as a starting point.

The four phonon transmission parameters, R_i^* and R_{ij}^* can be estimated using the acoustic mismatch model,[34] which was extended to stacks of layers in Ref. 35. Using this model we estimate for the phonon transmission coefficient across the Al/AlO$_x$/Al layers $\eta_{pe,ij}=0.068$. This value is almost the same for both samples, despite the difference in Al thickness. For the phonon losses from the base film into the sapphire substrate we estimate $\eta_{pl,1}=0.10$, while for the losses from the top film into the (few nm thick) NbO$_x$ layer that covers all our samples, the transmission coefficient is estimated to by $\eta_{pl,2}=0.16$. (Lacking phonon transmission data for the Nb/NbO$_x$ interface, we used data for the Nb/TiO$_2$ interface in Ref. 34.)

The parameters for quasiparticle losses across bridges connecting adjacent STJ's ($g_{l,i}$) are basically fixed by the cross-talk signals in the neighboring STJ's. So the only truly uncertain parameters are the quasiparticle loss rates at the edges (β_1 and β_2) and into leads and localized traps. Since these depend very much on processing conditions they can take on a broad range of values. These are the only parameters that really need to be fitted. Note that the rates $\Gamma_{l,i}$ are bulk quasiparticle loss rates, and do not include the more specific quasiparticle losses at the edges, through electrical connections and into localized traps. Thus, a change in $g_{l,i}$ or β_i immediately implies an opposite change in $\Gamma_{l,i}$ in order to maintain the correct charge output value.

As was made explicit in paper I, we can either have full spatial resolution at the expense of time dependence or have time-resolved information without spatial resolution. Because the combination of charge output and pulse duration for both electrodes provides enough information to determine the quasiparticle tunnel and loss rates in the two electrodes, we attempt to model the pulse duration times as well. To this end, model pulses are processed and calibrated in a way which mimics as closely as possible the processing of the current pulses described above. Therefore, the computed and measured values for the pulse duration time should be directly comparable. The quasiparticle tunnel and loss rates (four parameters) can now be estimated from the combination of charge output and pulse duration times in top and base films (four values) using the following dependences: Reducing simultaneously Γ_t and Γ_l by the same fraction hardly affects the charge output, but increases the pulse duration time via the dominating exponential factor in Eq. (E2) of paper I. On the other hand, an increase of Γ_t and a decrease of Γ_l such that their sum remains invariant, does not influence the pulse duration time [cf. the definitions of the exponential factors in Eq. (A2) of paper I], but does increase the charge output. Apart from the corrections due to quasiparticle losses at the edges and through leads and traps, we need to account for the effect of the electronic amplification and shaping on the measurement of the pulse duration. The computation of the pulse duration times therefore requires three additional ''fixed'' parameters: the fast and slow shaping times τ_{fast} and τ_{slow}, and the RC time of the preamplifier τ_{RC}.

2. Fitting strategies

The above five model components in Table II have been coded in IDL (Research Systems Inc.). The second iteration is by far the slowest step, and, as we will demonstrate below, of negligible importance in practical applications. For a given set of parameters, a typical evaluation of the response surface of an electrode, on a 50×50 grid, summing up to 50 harmonics, and omitting the second iteration, takes of the order of 100 seconds on a 300 MHz PC (whereas the evaluation of the second iteration step, summing up to 40 harmonics, will typically run for a day). This opens up the possibility of fitting model response surfaces to actual data. However, finding a best-fitting solution in a space spanned by 14 parameters is quite a challenge. The brute force approach of systematic variation of each parameter in an ac-

ceptable range is clearly excluded on computational grounds, no matter how efficient the routines are. More efficient search strategies such as a genetic algorithm[36] or the multidimensional downhill simplex method[37] are only a partial solution. In both cases we found that the bottleneck was not so much the search strategy itself, but the actual comparison of the model with the data. A single number that describes the quality of the fit, such as the usual χ^2 value, turned out not very useful for our more complicated datasets. First, the data do not only consist of spectra, but also of information about the pulse duration. It is arbitrary how much weight each of the components in the dataset should receive in the final figure of merit. Secondly, small spectral features, such as the K_β line from the thin base film, carry most information about the nonlinearity of the detector. Fitting strategies based on a single figure of merit completely missed these small features and therefore tend to wrongly estimate the associated phonon parameters. Instead of concentrating on more elaborate schemes to verify automatically the quality of the fit, we found it was feasible to perform the fit by hand. Starting from the above educated guesses about the values of the input parameters, we found it is possible to obtain satisfactory fits to the datasets in a couple of hours. In this approach the uniqueness of solution is not guaranteed; but neither is this true also for other numerical strategies, due to the arbitrariness of the figure of merit.

C. Two examples

Even without a detailed quantitative comparison to data, the model can provide very useful insight into ways of enhancing the performance of STJ's. One example was already given in paper I: if the tunnel and/or loss rates in an electrode could be tuned to render $\tilde{R}_{ij}=0$, the STJ response for photon absorption in that electrode becomes perfectly linear over the range of energies where second order effects are negligible. Admittedly, this requires a fine-tuning of tunnel and loss rates that is difficult to achieve in practice, because of the inherent inaccuracies of the fabrication process. Here we discuss two examples of possible improvements that are much easier to achieve, namely through the number and positioning of loss channels to the electrodes. The term loss channels does not apply only to lead or bridge connections, but also to local traps, whether deliberate or unintentional.

1. Number of loss channels

Figure 5 demonstrates what happens when bridges (with a throughput typical of a bridge connection of the array) are added one by one to an electrode with an otherwise ideal response. Going from one to two bridges has a markedly larger impact on the energy resolution than going from two to three bridges. At this stage, multiple peaks may arise in the spectral line, even though the input photons were assumed to be perfectly monochromatic. The surprise of this exercise, however, was in the last step, going from three to four bridges: The energy resolution in the case of four bridges turned out to be the same as in the situation where only one bridge was present, even though the charge output has dropped effectively by 20%. The explanation lies in the

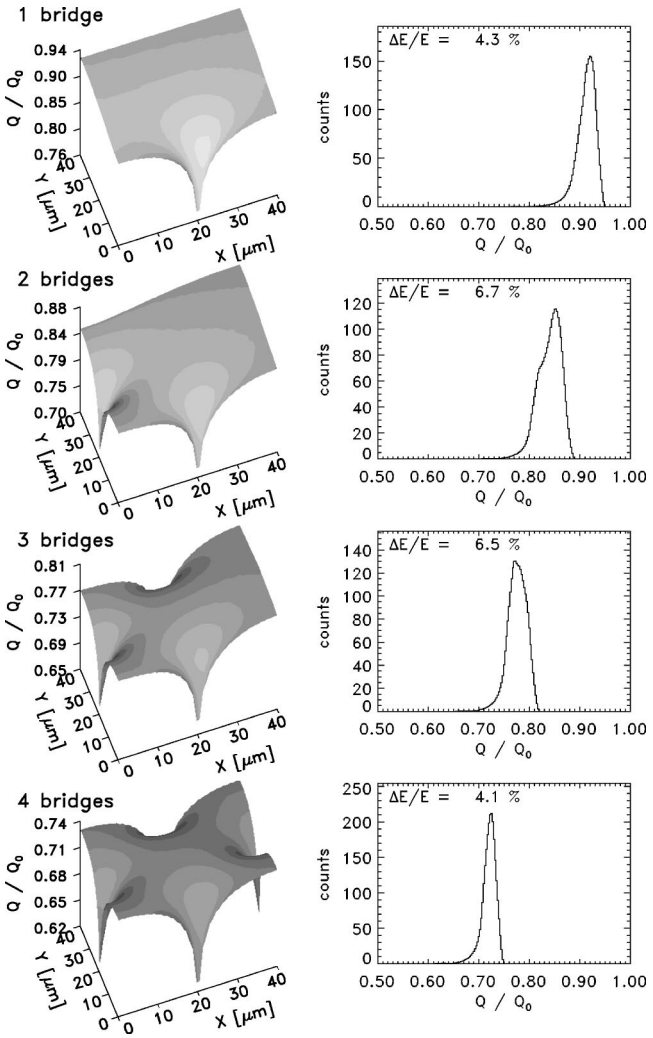

FIG. 5. The response surface due to the presence of an increasing number of bridges, and the corresponding spectral lines. The inset gives the FWHM spectral linewidth as a per cent fraction of the full signal.

symmetry of response surface. Adding one bridge to a situation in which already three bridges are present brings the topology of the response surface from an extremely asymmetrical situation back to the fourfold symmetry associated with a square electrode. Conversely, this figure implies that one-by-one removal of possible causes of resolution degradation (such as unintended local traps at the edge of an electrode) may occasionally work in the opposite direction. It also implies that the energy resolution of STJ's at the edge of an array will be considerably worse than that of STJ's which are completely surrounded by neighbors, unless they are supplemented with dummy bridges that cause a similar quasiparticle loss as the real bridges.

2. Position of a loss channel

Corners are more difficult to diffuse into than the sides of the electrode. This principle is illustrated with Fig. 6, where a single loss channel (again with a loss rate corresponding to a typical bridge in the array) is moved from the central side

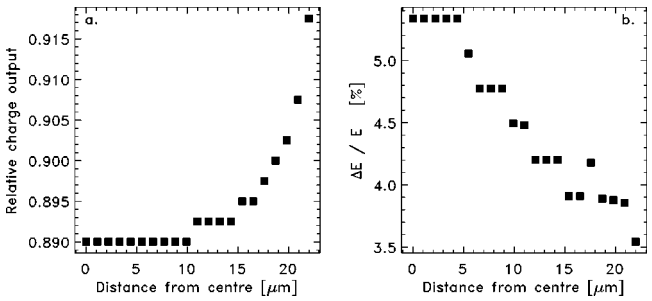

FIG. 6. The charge output and the FWHM spectral linewidth as a function of the location of the loss channel.

position to the corner. To minimize the impact on the charge output and energy resolution, the preferred position for a bridge or a lead is clearly as close as possible to the corner of the STJ. For single STJ's this configuration is also preferred for another reason: it is the most convenient position for placing an STJ in a 45° orientation with respect to the magnetic field in order to have maximum suppression of the Josephson current. For arrays the configuration is often different, but placing bridges in or close to the corners also promotes the performance of the STJ: Compared to the last example in Fig. 5, placing the four bridges in the corners does not so much improve the energy resolution, because the degree of symmetry remains the same, but the charge output may be improved by a few per cent up to well over 10%, depending on the parameter values.

IV. RESULTS

A. Sample 1: a series of single STJ's

There are three reasons why we chose to model this dataset. First, good quality LTSEM data was available for two STJ's on the chip. Second, there is a clear dependence of the energy resolution on the size of the STJ in both electrodes, which allows us to test the dependence of the energy resolution on the diffusive properties of the STJ's. And third, the range of electrode volumes spans two orders of magnitude, which allows us to test the assumptions for applicability of the linear superposition of perturbations of the response surface, on which our model is based.

Instead of modeling the entire LTSEM surface scan of the top electrode, we selected only the data on the diagonal that runs through the top and base lead connections (indicated as a white line in Fig. 2), because the response in these points is most affected by the diffusion of quasiparticles into the leads. The data on this line therefore contain most information about the value of the diffusion constant in the top electrode. The information on pulse duration times constrains the ratio between tunnel and loss times. The response surface of the 100 μm STJ is relatively insensitive to diffusion-related losses, so the spectral data for this device provide the strongest constraints on the actual values of quasiparticle tunnel and loss times. The β and Γ_l parameters for this device were kept in the same range as for the other devices. The phonon transport parameters were taken as predicted by the acoustic mismatch theory, and we found no reason to change them during the fitting. The data points in between top and base film are due to events in which the primary electron, ejected from the *K* shell after photon capture, crosses the barrier. These events were not modeled.

The values of the fitted parameters are listed in Table III, while the results of the fits are shown in Fig. 7 and Table IV. It is evident that the model is able to reproduce almost all the relevant features of the dataset: line shapes, relative line strengths, the shapes of the LTSEM scans, and the pulse duration times mostly to within a few percent. There are some exceptions, however, such as the position of the top-film line of the 50 μm STJ, and the pulse-duration time in the top film of the 100 μm STJ.

Most notably, the position of the Mn-$K\beta$ line detected by the base electrode of the 10 μm STJ is placed at a slightly too high charge relative to the Mn-$K\alpha$ line [Fig. 7(c)]. In this electrode one of the basic assumption for the applicability of the model $|S_2| \ll |S_1|$ does not apply, as can be seen in Table V, which lists the median values of (S_1) and (S_2) for a photon energy of 6 keV. Actually, it turned out that omitting both iteration steps gave a better match to the actual line position than inclusion of either the first or first two steps. So, while all other fitted curves in Figs. 7(c)–7(f) contain contributions from both first and second iterations, the fit to the base-film lines in Fig. 7(c) is made without any account of nonlinearity. As can be seen in Table V, the first and second iteration step are the first two terms of a series with alternating signs. In the case of the 10 μm base electrode this series is slowly converging to a relatively small contribution. Since the first few terms of this series are larger than

TABLE III. Parameters fit to the dataset of sample 1. Columns on the left describe parameters that are the same for all STJ's (related to the quality of the different layers and interfaces); columns on the right describe parameters that differ for individual STJ's (related to details of the fabrication process). Note that to facilitate comparison among the STJ's, the loss rate associated with the lead is listed, instead of the g_l parameter that characterizes the complete diffusion process.

electrode	D_j $\mathrm{cm^2\,s^{-1}}$	$\Gamma_{t,ij}$ $\mu\mathrm{s}^{-1}$	$\Gamma_{l,j}$ $\mu\mathrm{s}^{-1}$	R_j^* $\mu\mathrm{m^3\,s^{-1}}$	R_{ij}^* $\mu\mathrm{m^3\,s^{-1}}$	size μm	$\Gamma_{\mathrm{lead,top}}$ $\mu\mathrm{s}^{-1}$	$\Gamma_{\mathrm{lead,base}}$ $\mu\mathrm{s}^{-1}$	β_{top}	β_{base}
top	1.0	0.75	1.27	4.3	1.3	10	10.0	10^{-4}	0.11	0.022
base	50.	1.98	0.28	5.1	2.1	20	100.0	10^{-4}	0.29	0.025
						50	100.0	10^{-3}	0.34	0.064
						100	100.0	10^{-3}	0.10	0.070

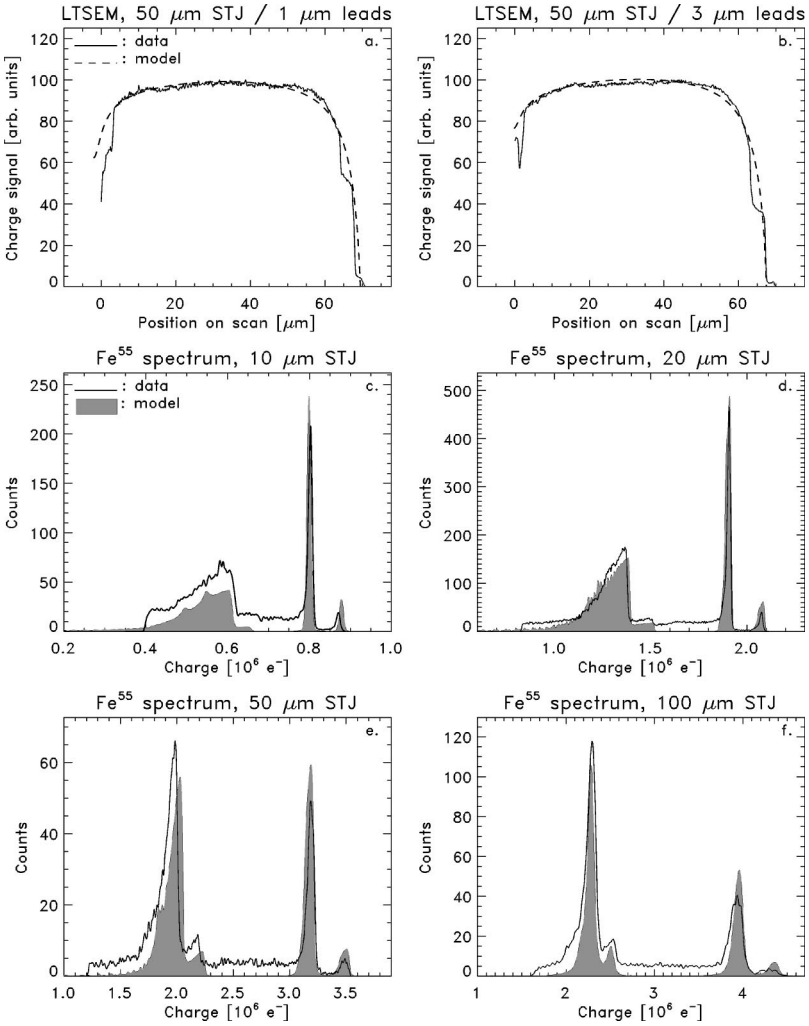

FIG. 7. (a), (b) Comparison between measured LTSEM scans and the modeled response for 50 μm STJ's (sample 1) with, respectively, 1 and 3 μm wide leads. The line scan was constructed by taking a cross cut of the surface scan along the diagonal parallel with the leads, as shown in Fig. 2. (c)–(f) Comparison between measured Fe^{55} spectra and model calculations for four STJ's, with sizes of, respectively, 10, 20, 50, and 100 μm and 1 μm lead widths. Solid lines represent measured spectra, filled gray histograms correspond to modeled spectra.

the total contribution, this implies that the intrinsic nonlinearity (due to quasiparticle self-recombination) in the 10 μm STJ is stronger than the nonlinearity derived from the spectral data. This means that recombination effects are partially compensated by quasiparticle tunneling and losses. Finally, we note that the (spectral) nonlinearity in the base films can, in principle, be completely removed if the ratio $\Gamma_{l,1}/\Gamma_{t,12}$ were increased by a factor 49.3, rendering $\tilde{R}_{12}=0$. The tunnelrate can be tuned by changing the thickness of the layers in the electrode, see, e.g., Ref. 38, and although the quasiparticle loss rate is less easily kept under control, this suggests a feasible cure for nonlinearity.

The diffusion constants found to fit the data are significantly smaller than the theoretical estimates above. From the RRR values of the electrodes, we would expect theoretical estimates for the diffusion constants of 12 and 327 $cm^2\,s^{-1}$, for top and base electrode, respectively. We found them to be a factor 6 – 12 smaller, although the ratio between the two values is not exactly the same as the ratio between the RRR values. The magnitude of the diffusion constants was not only restricted by the LTSEM data. An increase of the diffusion constants made it impossible to find a set of parameters with which all line shapes could be reproduced. In particular, for the top film it was difficult to reconcile the large line-

TABLE IV. Comparison between measured and fitted pulse duration times for single STJ's of different sizes (sample 1).

	Measured		Computed	
size	top	base	top	base
μm	μs	μs	μs	μs
10	0.34	0.28	0.43	0.24
20	0.56	0.53	0.65	0.54
50	0.84	0.77	0.87	0.80
100	1.01	0.91	0.67	0.95

TABLE V. Comparison of the (median) magnitude of the contributions from first and second iteration as a function of device size (sample 1).

size	Top electrode		Base electrode	
μm	first iter.	second iter.	first iter.	second iter.
10	-0.16	0.048	-0.26	0.21
20	-0.072	7.5×10^{-3}	-0.069	0.013
50	-0.044	1.8×10^{-3}	-0.015	4.5×10^{-4}
100	-0.039	1.1×10^{-3}	-7.8×10^{-3}	6.7×10^{-5}

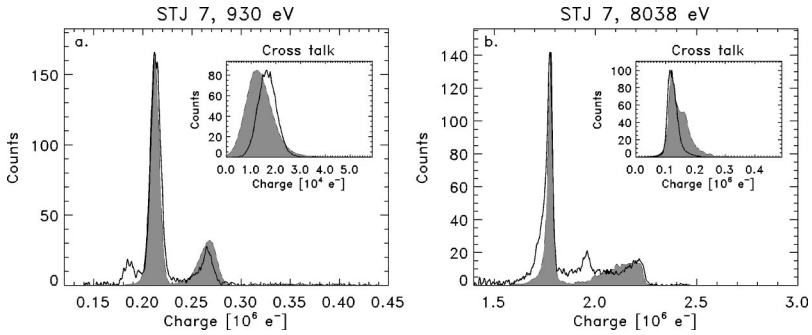

FIG. 8. Comparison between measured spectra obtained with STJ 7 of sample 2 and modeled spectra, at two energies Cu-*L* (930 eV) and Cu-*K* (8037 eV). The insets show the comparison between measured and modeled cross-talk across the bridges. The measured cross-talk spectra are constructed by averaging of the coincident signals in the two neighbor STJ's, 6 and 8. Solid lines represent measured spectra, filled gray histograms correspond to modeled spectra.

width for the smaller devices with the relative sharpness of the lines for the larger devices as the value of D_{top} was increased. Consequently, we are confident that the fitted values of the diffusion constants do indeed reflect a physical property of the STJ's.

B. Sample 2: an array of coupled STJ's.

In paper I it was shown that the problem of quasiparticle losses into leads, bridges and localized traps can be described by a single family of mathematical solutions, provided the loss channels are nonideal, in the sense that a certain fraction of the quasiparticles entering is lost. Sample 2 offers the possibility to quantify the properties of this family, which is characterized by a single parameter g_l (see Appendix C in paper I). By measuring in coincidence the charge signal in one STJ and the cross-talk signal across the bridges in its two neighbors, we can determine the losses through these bridges and other channels characterized by the same g_l parameter.

1. Spectral data

The spectral data to which we attempted to fit the model were acquired with STJ 7, and are shown in Fig. 8. Simultaneously, we tried to reproduce the features in Fig. 4, as well as the pulse duration times. Following the scheme outlined in Sec. III we arrived at the set of input parameters described in Table VI, and the pulse duration times listed in Table VII. The result is shown in Fig. 8 for two spectra, taken at the *L* and *K* lines of Cu.

Because in both cases the α and β component are 20 eV apart, we treat them separately in the model. So we model a spectrum with four components, the Cu-$L\alpha$ (920 eV) and $L\beta$ (940 eV) lines, and the Cu-$K\alpha_2$ (8027 eV) and $K\alpha_1$ (8047 eV) lines. The fixed parameters L, d_1, and d_2 are taken as described in Sec II. The summations were expanded into 25 harmonics, and r_{ini} was estimated to be 1 μm. The phonon transport parameters were taken as predicted by the acoustic mismatch theory, and kept constant during the fitting. Because the two spectra were taken in separate runs, the nonlinearity of the STJ at Cu-*K* must be separated from possible variations in the measured response. From our experience, the differences between measurements made during different cool downs is of the order of several per cent.

The model faithfully reproduces the main spectral details, relative line strengths and positions of the lines, while the pulse duration times are predicted to within 4%. Only the cross-talk line shapes appear somewhat wider than actually measured. Although the width of the Cu-*K* line measured by the base film is overestimated, the overal distribution of charge output and FWHM linewidths in Figs. 4(b) and 4(e) are satisfactorily accounted for, which was our main concern.

2. Cross talk

The cross-talk events are separated from substrate events (photon absorption events in the substrate mediated by phonons to the base electrode) by their coincidence with base or top electrode events in the neighbor STJ. In order to characterize the differences between the measured and the modelled cross-talk signal, we selected only cross-talk events originating in the top electrode, because this line is strongest and has the smallest width.

As the bridges are short, only 2 μm, the quasiparticle losses during passage are very small. We therefore assume that all the quasiparticle loss via these channels is due to diffusion into the neighbor electrode.

Because the cross-talk signal is much smaller than the original signal, it is much less subject to nonlinearity in the neighbor STJ for high-energy photons. It is, however, subject to nonlinearity in the STJ where the photon is absorbed, and is corrected accordingly. We found that even after this correction, the cross talk in the Cu-*K* spectrum was still overestimated, while it gave a good match in the Cu-*L* spectrum. Reducing the gain by 3% in the Cu-*K* spectrum, which is

TABLE VI. Parameters fitted to the dataset of sample 2.

electrode	D_j $\mathrm{cm^2\,s^{-1}}$	$\Gamma_{t,ij}$ $\mu\mathrm{s}^{-1}$	$\Gamma_{l,j}$ $\mu\mathrm{s}^{-1}$	R_j^* $\mu\mathrm{m^3\,s^{-1}}$	R_{ij}^* $\mu\mathrm{m^3\,s^{-1}}$	β_j	$g_{l,j}$ $\mu\mathrm{s}^{-1}$	$g_{\mathrm{trap},j}$ $\mu\mathrm{s}^{-1}$
top+1 μm top lead	4.5	0.67	1.54	2.2	0.65	0.0	0.012	
base+1 μm top lead	17.6	1.08	0.60	3.8	1.5	0.1	0.15	0.18
top+2 μm top lead	4.5	0.67	1.54	2.2	0.65	0.0	0.025	
base+2 μm top lead	17.6	1.08	0.60	3.8	1.5	0.1	0.15	0.015

TABLE VII. Comparison between measured and fitted pulse duration times at two different photon energies for STJ 7 (sample 2).

	930 eV		8038 eV	
	top	base	top	base
measured	0.76	0.76	0.74	0.74
computed	0.77	0.74	0.77	0.74

within the variation expected for run-to-run differences, gave the match shown in Fig. 8(b). We did not attempt to model the spectral feature associated with the rim, the part of the base film not covered by the top film, in particular because its shape differs strongly from a square electrode. The corresponding cross-talk spectrum in Fig. 9(a) is less well reproduced. Although solutions exist that better reproduce the data in Fig. 9, these fail to reproduce the results in Fig. 4, while the challenge was to find a set of parameters that was able to explain all aspects of this comprehensive body of data.

3. Energy resolution

The data in Fig. 4 initially raised two questions concerning the energy resolution in the array. On the one hand, ΔE_{base} and ΔE_{top} hardly depend on the number of bridges at all. Figures 4(c) and 4(f) do not indicate an obvious relation between the cross-talk across the bridges and the energy resolution. Apparently, the addition of a third bridge to the two bridges that are already present does not make much difference for the RMS spatial variations in the response of the base electrode. This interpretation is supported by the fact that collimation of the x rays to a beam with a 10 μm [full width at half maximum (FWHM)] footprint, aimed at the center of the electrode, improves ΔE_{base} by 80%. So a question arises: why does the addition of another source of inhomogeneity in the charge response not further degrade the energy resolution? The answer may be be found in a comparison of the topology of the response surface for the cases of two and three bridges shown in Fig. 5, where the resolutions hardly degrades by adding an extra bridge.

Another conclusion that can be drawn from Fig. 4(e) is that the width of the top lead does have a strong impact on ΔE_{base}. Apparently, the reduction of the top lead width by half, improves ΔE_{base} by 40%. Hence a second question—how can a top contact, that is only reached after the quasiparticles start tunneling and through which at most 2% of the quasiparticle can escape, have such a profound impact on the base-film energy resolution, whereas an additional bridge, across which 7% of the quasiparticles diffuse, does not seem to influence the energy resolution at all? Simulations with increasingly stronger losses through the top lead indicated that the top lead itself cannot be the explanation. It may be that the processing associated with the top lead also formed a trap in the base film.

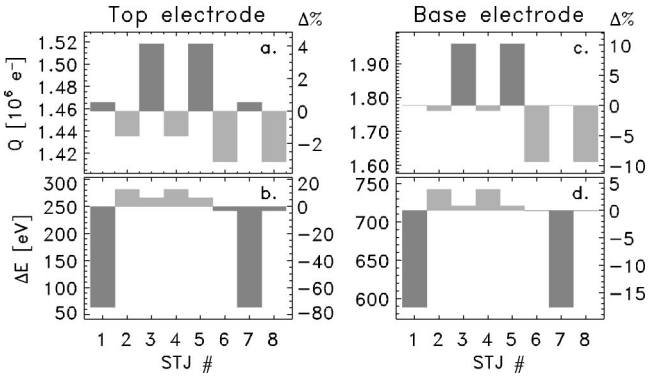

FIG. 9. Values for charge output and energy resolution for top and base electrodes derived from models of STJ's with different top-lead widths. To be compared to Fig. 4.

The trap had to be made quite strong, because a loss channel in a corner of the electrode affects the topology of the response surface much less than a loss channel located in the middle of one of the sides, as was shown in Fig. 6. Contrary to what we expected from the definition of the g parameter, the trap is strongest (by a factor 12) on the side of the smallest top lead width (see Table VI), so there is no obvious correlation with lead width. Considering that the 1 μm top leads are all on one side of the array (see Fig. 1), it might be that some sort of misalignment of one of the lithographic patterning masks could be at the origin of this problem.

In Fig. 9 we show modeled charge outputs and energy resolutions side-by-side for all eight working STJ's in the array. We find that the model accounts, at least qualitatively, for all these puzzling observations of the energy resolution as a function of the width of the top lead, in combination with the dependence of charge output on number of bridges. However, it was not trivial to find a set of parameters that properly explained the details of Fig. 4, and the patterns in Fig. 9 are very sensitive to the exact parameter values. In fact, we had to omit the convolution with the pulser signal to retain the similarity with Fig. 4. This casts some doubt on our simple explanation in terms of a single base-film trap associated with the top lead, but since the goal of this exercise was to demonstrate the capability of the model to reproduce comprehensive datasets, we did not venture into more complicated explanations, or more extensive searches of parameter space.

4. Nonideal edge

The base electrode of the STJ's in this array provides a good example of a nonideal edge as defined above. Since the base electrode is 4 μm larger than the top electrode, it contains a 2 μm wide rim from which quasiparticles cannot directly tunnel into the top electrode. During their stay in the rim, quasiparticles have a chance of getting lost, so the rim can be considered a nonideal reflecting edge. On average, the time spend by a quasiparticle in the rim will be $\tau_{\text{stay}} = w^2/4D_{\text{base}}$, where w is the width of the rim (2 μm), while the chance of getting lost is given by the bulk loss rate $\Gamma_{l,\text{base}}$, which was obtained from the fit to the data. Note that it was not necessary to introduce nonideal edges in the top electrode, hence we have set $\beta_{\text{top}}=0$. The reflectivity of the rim is given by $R=\exp(-\Gamma_{l,\text{base}}\tau_{\text{stay}})$. From the fitted value of the edge parameter $\beta=3L(1-R)/4\lambda$ we can derive the quasiparticle mean-free path λ in the base electrode to be 260 nm, a few times the electrode thickness. Since we expect

specular reflection of quasiparticles at the atomically flat interface between Nb and sapphire, and diffusive scattering at other interfaces, this seems indeed the right order of magnitude. Another check comes from scaling the λ at room temperature with the RRR value of the base electrode. Considering only Nb, we find $\lambda = 3$ RRR nm $= 183$ nm which is in good agreement with the value derived from the fitted β parameter. This is a strong confirmation of the validity of the model, since this link between β, $\Gamma_{l,\mathrm{base}}$ and D_{base} was not explicit in the model. It is also a confirmation of the existence of a bulk-loss component, even in a high-quality epitaxial film. Finally, we note that the expected contribution from recombination with thermal quasiparticles is over an order of magnitude smaller than the derived bulk-loss rate.

5. Diffusion constants

The diffusion constants obtained from the fit are again significantly lower than expected. Given the RRR values for base and top electrode of 41 and 8, we would expect diffusion constants of, respectively, 123 and 24 $\mathrm{cm}^2\,\mathrm{s}^{-1}$. In practice the diffusion in the base electrode is considerably smaller, by a factor of 7, while the diffusion constant in the top electrode is only a factor 5.5 smaller than expected. Again, the ratio of D_{base} to D_{top} is not equal to the ratio of the corresponding RRR values. This confirms that whatever the reasons for the slow quasiparticle transport in superconductors, they do not directly relate to the electron transport in the normal state.

Nevertheless, a comparison between Tables VI and III, listing, respectively, the parameters found in the fit to this dataset for sample 2 and the parameters fitted to the sample 1 data, shows a consistent pattern. First we note that judging from the RRR values the quality of the base film in the single STJ's is higher than that in the array. On the other hand, the quality of the top film appears lower. This is reflected in the values for the diffusion constants, and the bulk quasiparticle loss rates in Tables III and VI. Finally, we note that the ratio of the D_{base} in both samples does match the ratio between the corresponding RRR values, which installs further confidence in the fitted values for the diffusion constants.

V. CONCLUSIONS

We have tested the analytical model for the STJ response surface, developed in paper I, against two extended datasets that combined spectral data for multiple STJ's and pulse duration information, supplemented with LTSEM scans and cross-talk information. In both cases we had datasets that were large enough to place useful limits on most of the model parameters.

The model provides a close and detailed account of most of the features in the data, including the position, width, shape and relative strength of the spectral lines, the surface shape of the LTSEM scans, and the values for cross-talk signals and pulse-duration times.

The basic premises of the model were confirmed. In particular the requirements for weak nonlinearity $|S_1| \ll 1$ and $|S_2| \ll |S_1|$ are fulfilled in all STJ's we studied here, apart from the smallest device (10 μm in size) for which $|S_2| \lesssim |S_1|$, and more iteration steps are required. In this particular case, the subsequent iterations formed a slowly converging series of relatively large terms with alternating signs, resulting in a small total contribution. Skipping the iteration steps all together turned out to provide a more accurate description than including the first, or first two, iteration steps. This demonstrates that there is an important difference between the measured nonlinearity of a device, which follows from the charge output as a function of photon energy, and its intrinsic nonlinearity, which is related to the details of the quasiparticle recombination process.

We have demonstrated that the new concept of a superposition of separate contributions to the topology of the response surface is valuable for the characterization and understanding of detectors in which diffusion of the charge carriers plays a dominant role. In particular, in combination with analysis techniques such as LTSEM or the newly developed LTSSM, which directly probe the response surface, our model provides a powerful tool in the analysis and solution of problems with energy resolution in STJ's. But we are confident that the techniques developed in this work are useful in a much wider range of applications. Because of its computational speed this method is in principle suited for application in automatic fitting algorithms, although the uniqueness of any solution is hard to verify, due to the number of free parameters.

The solutions we obtained in both cases indicate that the quasiparticle diffusion constants in both electrodes are typically an order of magnitude smaller than the theoretical values, in accordance with the findings of other groups. We emphasize that it was not possible to find solutions with larger diffusion constants that fitted the data any near as well as the present ones. Neither was it possible to obtain solutions of the same quality in which the ratio of D_{base} to D_{top} matches the ratio of the corresponding RRR values. On the other hand, the ratio between the D_{base} in both samples does reflect the ratio of the RRR values of the epitaxial films in both samples, confirming the values of the fitted diffusion constants. It also demonstrates that quasiparticle diffusion through an epitaxial film is physically distinct from diffusion through a polycrystalline film. This seems to imply a relation between the quasiparticle and normal-state diffusion constant that goes beyond current theoretical models.

Contrary to what one might expect, the losses through the leads and at the edges do not fully account for the total quasiparticle loss budget. There remains a bulk loss component, even in the epitaxial base electrodes, which correlates with the quality of the film, as measured by the RRR values. We suspect that this bulk loss of quasiparticles also plays a role in the difference between normal-state and quasiparticle diffusion. This bulk loss is at least an order of magnitude larger than the expected contribution from recombination with thermal quasiparticles.

We would like to emphasize that our model goes beyond a mere description of data. Based on the examples we discussed, the results obtained with our model suggest qualitative guidelines for the improvement of the performance of high-resolution STJ detectors. It was one of the objectives of this paper to demonstrate that, provided a comprehensive set

of measurements of a series of STJ devices fabricated on the same chip has been made, one can put useful restrictions on the values of all these adjustable parameters. These adjustable parameters are primarily related to fabrication conditions (e.g., the quasiparticle diffusion constants, quasiparticle loss parameters, phonon parameters), and should be reproducible in future fabrication runs. Details of the design, on the other hand, are mainly related to what we have called the fixed parameters of the model (e.g., the size of the STJ, position and width of leads, etc.). The only design parameter to which most of the adjustable parameters are related to, the thickness of the layers, has a linear influence on their values. So, once a fit has been made, it is possible to predict results for future designs in a straightforward manner, and thus to optimize the design in a systematic way. We could already identify some general rules.

(a) It was shown that the position of leads and bridges has a strong influence on the contribution to the energy resolution: corners are the best locations for a lead, the center positions on the sides are the worst. Also, as losses through leads scale with their width, losses can be minimized by making the leads as small as possible.

(b) It would even be better if the influence of bridges and leads could be eliminated altogether, as they give, at least in the examples discussed, the strongest contribution to the inhomogeneity of the response surface. This could be achieved by fabricating them from higher energy-gap materials, but this turns out to be quite a challenge in practice.[3] The energy gap in short bridges between adjacent STJ's are reduced by the proximity of the lower-gap electrode material, and the energy of quasiparticles is raised above the local gap by Joule heating during tunneling. Furthermore, any additional step in the fabrication process increases the risk of the creation of additional quasiparticle trapping sites.

(c) In sample 1, we found that an increase of the ratio $\Gamma_{l,1}/\Gamma_{t,12}$ (in this case by a factor 50) would render the energy response of the base electrode of these detectors extremely linear (i.e., $\tilde{R}_{12}=0$). Although challenging to realize in practice, such a modification would be very interesting for small devices, in which nonlinear effects are strongest. For every electrode it is, in principle, possible to tune the loss and tunnelrates in such a way that they fully compensate the quasiparticle self-recombination.

(d) Perhaps the most important lesson was that in order to significantly improve the energy resolution all localized contributions that break the symmetry of the response surface (such as localized traps, leads, bridges) must be eliminated together. As we saw, from the point of view of energy resolution it is better to have four bridges on the STJ's in an array, than two or three. This is because with four bridges, the response surface is more symmetrically disturbed than in the case of two or three. So, removing one source of trouble, e.g., a trap at the edge caused by a flaw in the fabrication process, may not necessarily improve the energy resolution, and could actually have an adverse effect, depending on the topology of the response surface. This could explain why improving the energy resolution of STJ's to the statistical limit has proven to be such a persistent problem over the past decades.

ACKNOWLEDGMENTS

We gratefully acknowledge the assistance of Hans le Grand and Jens Martin with the LTSEM analysis at Tübingen University. The single STJ detector discussed in this paper was produced by the Oxford Instruments Scientific Research Division, Cambridge, UK, and the STJ detector array was manufactured by VTT Electronics, Espoo, Finland.

[1] C.A. Mears *et al.*, Nucl. Instrum. Methods Phys. Res. A **370**, 53 (1996).
[2] P. Verhoeve, N. Rando, A. Peacock, A. van Dordrecht, and D.J. Goldie, Appl. Phys. Lett. **72**, 3359 (1998).
[3] R.H. den Hartog *et al.*, Proc. SPIE **4012**, 237 (2000).
[4] G. Angloher *et al.*, Nucl. Instrum. Methods Phys. Res. A **444**, 214 (2000).
[5] U. Fano, Phys. Rev. **72**, 26 (1947).
[6] D.J. Goldie, P.L. Brink, C. Patel, N.E. Booth, and G.L. Salmon, Appl. Phys. Lett. **64**, 3169 (1994).
[7] C. Mears, S.E. Labov, and A. Barfknecht, Appl. Phys. Lett. **63**, 2961 (1993).
[8] A.G. Kozorezov, J.K. Wigmore, R. den Hartog, D. Martin, P. Verhoeve, and A. Peacock, preceding paper, Phys. Rev. B **66**, 094510 (2002).
[9] M.L. van den Berg *et al.*, IEEE Trans. Appl. Supercond. **7**, 3363 (1997).
[10] O.J. Luiten *et al.* (unpublished).
[11] M.L. van den Berg, Ph.D. thesis, Utrecht University, 1999.
[12] R. Christiano *et al.*, J. Appl. Phys. **86**, 4580 (1999).
[13] L. Parlato *et al.*, Nucl. Instrum. Methods Phys. Res. A **440**, 15 (2000).
[14] R. Gross and D. Koelle, Rep. Prog. Phys. **57**, 651 (1994).
[15] S.P. Lemke, Ph.D. thesis, Tübingen University, 1995.
[16] J. Martin *et al.*, Nucl. Instrum. Methods Phys. Res. A **370**, 88 (1996).
[17] H. Pressler, M. Ohkubo, M. Koike, T. Zama, T. Nakamura, and M. Katagiri, Appl. Phys. Lett. **77**, 4055 (2000).
[18] A. Peacock, Physica B **263–264**, 595 (1999).
[19] M. Gurvitch, M.A. Washington, H.A. Huggins, and J.M. Rowell, IEEE Trans. Magn. **MAG-19**, 791 (1983).
[20] J.M. Lumley, R.E. Somekh, J.E. Evetts, and J.H. James, IEEE Trans. Magn. **MAG-21**, 539 (1985).
[21] A. Kozorezov *et al.*, Phys. Rev. B **61**, 11807 (2000).
[22] J.K. Wigmore, A.C. Steele, A.G. Kozorezov, A. Peacock, R. den Hartog, and P. Verhoeve, Physica B (to be published); J. Appl. Phys. (to be published).
[23] G. Hölzer, M. Fritsch, M. Deutsch, J. Härtwig, and E. Förster, Phys. Rev. A **56**, 4554 (1997).
[24] B.L. Henke, P. Lee, T.J. Tanaka, R.L. Shimabukuro, and B.K. Fujikawa, At. Data Nucl. Data Tables **27**, 1 (1982).
[25] S. Kaplan *et al.*, Phys. Rev. B **14**, 4854 (1976).
[26] H.W. Weber *et al.*, Phys. Rev. B **44**, 7585 (1991).

[27] C.M. Soukoulis and D.A. Papaconstantopoulos, Phys. Rev. B **26**, 3673 (1982).
[28] V. Narayanamurti, R.C. Dynes, P. Hu, H. Smith, and W.F. Brinkman, Phys. Rev. B **18**, 6041 (1978).
[29] G.M. Eliasberg, JETP Lett. **11**, 114 (1970).
[30] A. Poelaert, A. Golubov, A. Peacock, R. den Hartog, and H. Rogalla, Nucl. Instrum. Methods Phys. Res. A **444**, 55 (2000).
[31] Th. Nussbaumer *et al.*, Phys. Rev. B **61**, 9719 (2000).
[32] S. Friedrich *et al.*, Appl. Phys. Lett. **71**, 26 (1998).
[33] M.L. van den Berg *et al.*, IEEE Trans. Appl. Supercond. **9**, 2951 (1999).
[34] S. Kaplan, J. Low Temp. Phys. **37**, 343 (1979).
[35] A. Poelaert, A. Peacock, N. Rando, P. Verhoeve, and P. Videler, J. Appl. Phys. **79**, 2574 (1996).
[36] D. E. Goldberg, *Genetic Algorithms in Search and Optimization* (Addison-Wesley, New York, 1989).
[37] W.H. Press, S.A. Teukolsky, W.T. Vetterling, and B.P. Flannery, *Numerical Recipes in Fortran*, 2nd ed. (Cambridge University Press, Cambridge, 1992).
[38] A. Poelaert, P. Verhoeve, N. Rando, A. Peacock, D.J. Goldie, and R. Venn, Proc. SPIE **2808**, 523 (1996).